Lawrence Berkeley National Laboratory

LBL Publications

Title

Stress-Induced Structural Transformations in Au Nanocrystals

Permalink

https://escholarship.org/uc/item/9xp9j24d

Journal

Nano Letters, 20(10)

ISSN

1530-6984

Authors

Parakh, Abhinav

Lee, Sangryun

Kiani, Mehrdad T

et al.

Publication Date

2020-10-14

DOI

10.1021/acs.nanolett.0c03371

Peer reviewed

eScholarship.org Powered by the California Digital Library
University of California

Stress Induced Structural Transformations in Au Nanocrystals

*Abhinav Parakh[1], Sangryun Lee[2], Mehrdad T. Kiani[1], David Doan[3], Martin Kunz[4], Andrew Doran[4], Seunghwa Ryu[2] and X. Wendy Gu[3]**

[1]Materials Science and Engineering, Stanford University, Stanford, CA 94305, USA.

[2]Mechanical Engineering, KAIST, Yuseong-gu, Daejeon 34141, Republic of Korea.

[3]Mechanical Engineering, Stanford University, Stanford, CA 94305, USA.

[4]Advanced Light Source, Lawrence Berkeley National Lab, Berkeley 94720, USA.

Abstract: Nanocrystals can exist in multiply twinned structures like icosahedron, or single crystalline structures like cuboctahedron. Transformations between these structures can proceed through diffusion or displacive motion. Experimental studies on nanocrystal structural transformations have focused on high temperature diffusion mediated processes. Limited experimental evidence of displacive motion exists. We report structural transformation of 6 nm Au nanocrystals under nonhydrostatic pressure of 7.7 GPa in a diamond anvil cell that is driven by displacive motion. X-ray diffraction and transmission electron microscopy were used to detect the structural transformation from multiply twinned to single crystalline. Single crystalline nanocrystals were recovered after unloading, then quickly reverted to the multiply twinned state after dispersion in toluene. The dynamics of recovery was captured using TEM which showed surface recrystallization and rapid twin boundary motion. Molecular dynamics simulations showed that twin boundaries are unstable due to defects nucleated from the interior of the nanocrystal.

Keywords: Diamond Anvil Cell, X-ray Diffraction, Transmission Electron Microscopy
Molecular Dynamics Simulation, Asymmetric Mackay-like Transformation

Main Text:

Metallic nanocrystals are used widely in fields such as photonics, biomedical therapies, catalysis, electronics and sensing[1]. Properties of these nanocrystals are highly dependent on their size, shape, and crystalline structure[2]. Multiply twinned (MT) icosahedron, MT decahedron, single-crystal (SC) cuboctahedron, and SC Wulff-polyhedron nanocrystal shapes are commonly observed, and can have different catalytic, magnetic, mechanical, structural, and electronic properties[3–8]. For this reason, it is often desirable to synthesize one particular nanocrystal size and shape, and maintain this structure during use. This remains difficult because the thermodynamic stability and structural transitions between different nanocrystal structures are still incompletely understood. The structural transformation of polyhedral structures such as MT icosahedron is also important for understanding materials like metallic glasses and magnetic nanoclusters, in which polyhedral atomic clusters make up the basic structural unit, and changes in these atomic clusters dictate material properties[9–11].

Structural transformation between different nanocrystal shapes have been studied using theory, simulations, and experiments. Using energy balance calculations and molecular dynamics (MD) simulations that consider differences in surface energy and lattice strain, it has been determined that MT nanocrystals are stable at smaller sizes and SC nanocrystals are stable at larger sizes[9,12–14]. The transition occurs from 2 to 10 nm depending on the calculation method, and varies in experiments due to the influence of surface ligands, solvents and substrates on surface energy. It has been proposed that the transformation between MT and SC structures

occurs through diffusive or displacive processes, such as surface melting and restructuring, dislocation/disclination activity, and the symmetric and asymmetric Mackay-like transformation[15–19]. Transformation in nanocrystals have been studied experimentally by heating nanocrystals with the electron beam in a transmission electron microscope (TEM), high energy laser pulses, and annealing nanocrystals on a substrate[16,17,20–23]. These experimental studies observed that enhanced mobility, melting and recrystallization of nanocrystals lead to diffusion mediated structural transformations. However, displacive motion mediated structural transformation has not been studied systematically in nanocrystals.

High-pressure compression in a diamond anvil cell (DAC) is an ideal technique to study displacive motion in nanomaterials, because diffusion is suppressed at high pressure[24]. DAC has previously been used to study high-pressure phase transformation, crystallization and sintering of aggregated nanocrystals[25]. DAC techniques have also been used to study structural transformations in Ag nanocrystals under hydrostatic pressures,[26] which minimizes both diffusion and displacive motion. Here, we study the structural stability and structural transformation between MT and SC nanocrystals by compressing 6 nm Au nanocrystals in a DAC under non-hydrostatic pressure, and monitoring nanocrystal structure using *in situ* X-ray diffraction (XRD). The nanocrystals are recovered after compression and imaged using TEM. We find that the 6 nm nanocrystals undergo a MT to SC transformation after compression to 7.7 GPa of pressure. This is in contrast to smaller, 3.9 nm Au nanocrystals which did not show a structural transformation under pressure, and instead formed stacking faults via surface nucleated partial dislocations[27]. MD simulations were conducted to understand defect formation in nanocrystals of 3.9 nm and 6 nm in size. These simulations showed that dislocation activity is enhanced in larger nanocrystals.

These results indicate that displacive motion driven large scale structural transformation is possible in nanocrystals and must be considered in designing structures at the nanoscale.

MT Au nanocrystals were synthesized using organic phase reduction of chloroauric acid and capped with dodecanethiol ligands[28]. The nanocrystal size distribution was found to be 6.0±0.3 nm using TEM (see Fig. 1A and Fig. S1). High-resolution TEM images showed that the majority of nanocrystals (~80%) were MT and remaining nanocrystals were SC (a total of 59 nanocrystals were analyzed). The MT nanocrystals were icosahedral structures which are formed with 20 tetrahedral units joined by 20 twin boundaries. An icosahedral polyhedron has 6 5-fold, 10 3-fold, and 15 2-fold axes. Fig. 1B shows the icosahedral nanocrystal along the 3-fold axis and Fig. 1C shows the icosahedral nanocrystal along a 2-fold axis. The SC nanocrystals were cuboctahedron or Wulff-polyhedron in structure, and sometimes contained 1-2 twin boundaries rather than the high density of twin boundaries in MT nanocrystals.

Ambient pressure XRD for the nanocrystals showed an FCC crystal structure, and significantly broader peaks than bulk Au due to crystallite size broadening (see Fig. S2). Nanocrystal surfaces exert a Laplace pressure on the interior of the nanocrystal, which scales inversely with the radius[29]. This compressive force shifts all the ambient pressure XRD peaks except the (200) peak to a higher 2θ angle compared to the bulk. The {111} planes form the surface of MT icosahedral nanocrystals. Hence, the (111) peak was shifted by ~0.06^{o} 2θ compared to the bulk, which corresponds to a volumetric strain of ~1.5%. The position of the (200) peak does not shift in the same way as the other peaks because it is affected by twinning in the nanocrystal. This was previously shown in a model which revealed that the (200) peak shifts towards lower 2θ angles with an increase in twinning density[30,31]. This model simulates the effect of low twinning density and cannot be directly applied to MT nanocrystals which each contain 20 twins, but the qualitative trend is still relevant. Another feature of the (200) peak is the double peak which is due to the mixture of 80% MT and 20% SC nanocrystals. One peak is located at

93 the bulk (200) peak position, and the other is shifted towards lower 2θ angles by ~0.6^0 2θ. The
94 icosahedral nanocrystals correspond to the lower 2θ (200) peak, which is shifted due to the twins,
95 and the SC nanocrystals correspond to the (200) peak at the bulk position.

96 High-pressure XRD was obtained *in situ* during DAC compression experiments at the
97 Advanced Light Source at Lawrence Berkeley National Laboratory. Toluene was used as the
98 pressure medium and toluene becomes non-hydrostatic above 1.9 GPa pressure[32]. The
99 nanocrystals were loaded as a thick film at the bottom of the DAC sample chamber. XRD was
100 collected while the nanocrystals were loaded up to 7.7 GPa and as pressure was released. The
101 pressure was limited to 7.7 GPa to avoid sintering between the nanocrystals, which has been
102 observed at higher pressures[33–35]. The XRD peak position and width (full width at half maximum)
103 were observed to change with increasing and decreasing pressure and were quantified at each
104 pressure (Fig. 2).

105 High-pressure XRD and the corresponding peak positions and widths are shown in Fig.
106 2. The shift in XRD peak position indicates the pressure-induced elastic strain in the
107 nanocrystals. XRD peak position for all peaks except the (200) peak recovered completely with
108 pressure cycling to within 0.1% of their original value (Fig. 2 D). An irreversible change was
109 observed for the (200) peak position with pressure cycling (Fig. 2 B). The ratio of the left to the
110 right (200) peak intensities is proportional to the degree of twinning, or the fraction of MT to SC
111 nanocrystals in the sample[30]. After pressure cycling, this ratio decreased by ~22%: the right (200)
112 peak intensity increased significantly with pressure and remained at higher values after
113 unloading, while the left (200) peak decreased in intensity. This indicated that the MT
114 nanocrystals detwinned with pressure cycling and underwent a structural transformation from
115 MT to SC. Changes in peak width with pressure cycling also indicate that this structural

transformation occurred (see Fig. 2 C). The XRD peak width for (111), (220) and (311) peaks decreased by 11%, 19%, and 22%, respectively. This can be explained by an increase in crystallite size upon transformation from MT to SC nanocrystals[36].

Post-compression TEM imaging corroborated these findings. Nanocrystals were loaded to ~5 GPa in the DAC. The sample was then quickly unloaded, and the sample chamber was opened to air to dry out the liquid toluene. The nanocrystals were picked up using a needle and scraped onto a TEM grid and inserted into the TEM within 10 minutes. The post-compression TEM images are shown in Fig. 3. We found that the ratio of nanocrystals changed from 80% MT and 20% SC nanocrystals before pressure cycling, to 40% MT and 60% SC nanocrystals after pressure cycling. The fraction of MT nanocrystals decreased by 50% with pressure cycling. High-resolution TEM images of 59 as-synthesized and 23 post-compression nanocrystals were analyzed. Post-compression nanocrystals were SC with cuboctahedron, truncated-octahedron or Wulff-polyhedron shapes (Fig. 3). Some SC nanocrystals had a twin that extended across the nanocrystal (Fig. 3 B). Using the ratio of MT to SC nanocrystals from TEM, the Debye scattering equation was used to simulate pre- and post-compression XRD patterns. Fig. S4 shows the simulated XRD pattern for mixtures of 80:20 and 40:60 MT and SC nanocrystals. The simulated XRD pattern showed similar trends as the experimental XRD patterns, in which the ratio of the left and right (200) peaks decreased with decreasing fraction of MT nanocrystals. This showed that the post-compression TEM analysis matches the high-pressure XRD patterns.

The post-compression SC structure of the nanocrystal was observed to be unstable. Toluene was added drop by drop to a TEM grid with post-compression nanocrystals. TEM imaging was performed after waiting for 10-15 mins, which showed that the ratio of MT to SC structures reverted close to the as-synthesized value (85% MT and 15% SC, 48 nanocrystals

analyzed). This showed that the nanocrystal can rapidly convert to the thermodynamically stable MT structure in solution at ambient pressure (see Fig. S5). The dynamics and mobility of twin boundaries in nanocrystals was further investigated by heating individual nanocrystals under a 200 keV electron beam within the TEM. TEM movie and snapshots of the nanocrystal coalescence process[37–40] is shown in Supplementary Movie S1 and Fig. 4. At the start of the movie, nanocrystal I is 7 nm in size and has two visible inclined twin boundaries at 35°. Nanocrystal II is 6.3 nm in size and has a MT structure (Fig. 4 A). Fig. 4 B, C and D show the nanocrystals after 10 s, 40 s and 70 s of electron beam irradiation, respectively. After 10 s, nanocrystal I rapidly developed a MT structure in the lower half of the nanocrystal, and the angle between the twin boundaries increased to ~70°. The surface of nanocrystal I started melting and sintering with the nanocrystal II. After 40 s, the surface of nanocrystal II started melting and nanocrystal II rotated to sinter with the nanocrystal I. The twin boundaries in nanocrystal I dynamically moved away from the sintered part of the nanocrystal. Fig. 4 D shows final state of the nanocrystals. A SC region connects both nanocrystals. The nanocrystal I has a MT structure with the twin boundaries at an angle of ~71° which is close to the ideal ~72° for a strained penta-twinned structure. This showed that the twin boundaries in nanocrystal can evolve due to enhanced diffusion under excitation by the electron beam. It is likely that the enhanced mobility of twin boundaries and interaction of ligands/surface of the nanocrystal with toluene solvent resulted in the rapid recovery of MT structure from SC nanocrystal in solution. The post-compression TEM and high-pressure XRD analysis confirmed that the MT 6 nm nanocrystals transformed into SC nanocrystals with pressure cycling, and the SC structure was unstable at ambient pressure and reverted back to MT structure after leaving in solution for short time.

The high-pressure behavior of 6 nm nanocrystals differs from that of 3.9 nm nanocrystals previously studied by our group[27]. High pressure experiments for 3.9 nm nanocrystals showed that all the XRD peak positions including the (200) peak recovered with pressure cycling to within 0.2% of its original value (see Fig. S6). The complete recovery of the (200) peak position indicated that the MT structure of the 3.9 nm nanocrystal was preserved with pressure cycling. In addition, the XRD peak widths for 3.9 nm nanocrystals showed the opposite trend as for 6 nm nanocrystals. The 3.9 nm XRD peak widths for (200) and (220) peaks increased by 16% and 23%, respectively, and remained at higher values after unloading. The peak width for (111) plane remained at about 2% of its initial value with pressure cycling. This indicated the introduction of surface nucleated partial dislocations (stacking faults) with pressure cycling.

The size-dependent MT to SC structural transformation can be analyzed in terms of the thermodynamic stability of the two structures. Howie and Marks represented the energy of a nanocrystal as:[41]

$$U = W_s + W_\gamma + W_{el} + H(V) \quad (0)$$

Where W_s, W_γ, W_{el} and $H(V)$ are the energy due to surface stress, energy due to strain in the surface, elastic strain energy due to applied external pressure and nanocrystal geometry, and cohesive energy, respectively. Using this approach, it is found that the MT structure is stable at smaller sizes, the SC structure is stable at larger sizes and that the MT structure transforms into SC structure at a critical nanocrystal size of 7.2 nm at ambient pressure. At high pressure, the elastic strain energy and energy due to strain in the surface is modified to include additional energy input from the external pressure (see supplementary information). The transition size reduces with increasing pressure (see Fig. S7) and is 5.4 nm at 7.7 GPa (the maximum applied

pressure in the experiments). This shows that it is thermodynamically favorable for 6 nm nanocrystals to be SC at high pressure, while it is favorable for 3.9 nm nanocrystals to be MT.

Similarly, MD simulations have shown that the MT structure is stable at smaller sizes and the SC structure is stable at larger sizes[9,13,14,42]. The MT structure transforms into the SC structure at a critical nanocrystal size of ~2-5 nm depending on the interatomic potential. This transition reflects the lower surface energy and higher lattice strain of MT structures. At high pressures, the MT structure is unfavorable compared to the SC structure due to its lower atomic packing fraction[19].

Next, we consider the atomistic mechanism of the MT to SC transition at high pressure. Transformations in nanocrystals can occur through surface diffusion mediated mechanisms at elevated temperatures[21,22]. Diffusion is suppressed at high pressure and cannot be the mechanism for the MT to SC transformation in the nanocrystals[24]. At high pressure, the transformation can occur through a nondiffusive Mackay transformation or a dislocation/disclination mediated detwinning process. The Mackay transformation is displacive atomic motion driven MT icosahedron to SC cuboctahedron transformation which can proceed through symmetric[19] or asymmetric paths[15] (Fig. S8). The Mackay transformation requires low activation energy[43–45]. Simulation studies predict the dynamics of transformation using total energy calculation along the Mackay path[15,43,46,47] or MD simulations for small nanocrystals[48–50]. Symmetric Mackay transformation is not compatible with deviatoric stresses however, the asymmetric Mackay-like transformation can be driven by deviatoric stresses. The MT to SC structural transformation can also proceed through dislocation or disclination mediated detwinning. Dislocation mediated detwinning was previously observed in large Pt nanocrystal under oxidative heating[17]. The SC grain nucleated at the surface of the nanocrystal and then grew when dislocation motion led to

the retraction of twin boundaries. This transformation has also been observed to occur through the motion of disclinations[18].

The MT to SC transition is driven by deviatoric stresses caused by the nonhydrostatic pressure medium. The stress in the nanocrystals is higher along the loading axis (and the direction of imaging) than in the transverse direction. The difference between axial and transverse stress is termed differential stress. Differential stress in the sample chamber can be estimated using the lattice strain theory for FCC metals[51]. The maximum differential stress in 6 nm nanocrystals was ~2 GPa (see Fig. S9). We have previously shown that 3.9 nm nanocrystals can sustain dislocation activity due to the deviatoric stresses, while sustaining its twin boundary structures[27]. In order to understand the size-dependent stability of twin boundary structures, we performed MD simulations of 3.9 nm and 6 nm icosahedral nanocrystals (Fig. 5). Although the direct observation of structural transformation was not accessible in MD simulation due to the limited timescale, we were able to quantify the size-dependent pre-stress and to discover different twin boundary stabilities in small and large nanocrystals. While the angle between two non-parallel {111} surfaces is 70.53° in bulk FCC crystals, the twin boundaries in icosahedral nanocrystals form a 72° angle due to the five-fold symmetry, which inevitably induces pre-stress from the mismatch strain. The mismatch strain and resulting pre-stress inside icosahedral and decahedral MT nanocrystals can be approximated by the superposition of multiple finite-length disclinations. By assuming elastic isotropy and spherical surface, the pre-stress distribution inside MT icosahedral nanocrystal can be approximated as follows (see supplementary information).

$$\sigma_{rr} = \frac{4\mu\epsilon_I}{3}\left(\frac{1+\nu}{1-\nu}\right)\ln\left(\frac{r}{R}\right) - P \qquad (2)$$

where $\epsilon_I = 0.0615$, μ is the shear modulus, ν is the Poisson's ratio, R is the radius of the nanocrystal, P is the external pressure, and r, θ and ϕ are the spherical coordinates. The solution indicates pure compressive stress along the radial direction. The maximum value of compressive stress is found to be higher in the larger nanocrystal. Smaller nanocrystals are subjected to higher average strain energy and larger hydrostatic compression due to higher Laplace pressure from surface stress[41]. This is consistent with our ambient pressure XRD measurement where 3.9 nm shows a larger shift in the (111) peak position. Even though the theoretical analysis omits elastic anisotropy, the analytical solution with $\ln \frac{r}{R}$ dependence matches qualitatively well with the atomic potential energy distribution depicted in Fig. 5 B, which shows that 3.9 and 6 nm nanocrystals have higher strain energy density near the core and 6 nm nanocrystal has larger maximum atomic potential energy (i.e. higher pre-stress). Defect nucleation from the pristine twin structure is likely to initiate from the region of high pre-stress, so it is expected that defect nucleation occurs preferentially near the core of the MT nanocrystal. The MT structure in the larger nanocrystal is more susceptible to defect nucleation near the core because of its higher maximum pre-stress and can sustain pre-existing dislocations at ambient pressure. The twin boundary structures with five-fold symmetry become progressively unstable for larger MT nanocrystals. We found that, even in the absence of any external stimuli, dislocation nucleation and distortion of twin boundaries were observed in 6 nm icosahedral nanocrystal in vacuum under relatively long high temperature MD simulation, while neither dislocation activity nor distortion of twin boundary structure is observed in the 3.9 nm nanocrystal due to smaller pre-stress (Fig. 5 C). These unstable twin boundary structures and pre-existing defects allow

deviatoric stress on the 6 nm MT nanocrystal to drive the asymmetric Mackay-like transformation or dislocation/disclination mediated detwinning.

In summary, we have used high-pressure XRD and post-compression TEM to provide the first evidence of deviatoric stress induced MT to SC structural transformation in nanocrystals. Energy calculations showed that the 6 nm MT nanocrystals become unstable at high pressures and the critical size for transition between MT and SC nanocrystals reduces with increasing pressure. MD simulations showed that the 6 nm MT nanocrystal was more susceptible to dislocation nucleation, had unstable twin boundaries and can have pre-existing dislocations. Deviatoric stress driven kinetics of the process is governed by two possible paths – asymmetric Mackay-like transformation or dislocation/disclination mediated detwinning. High-pressure SC nanocrystals were recovered after unloading, however, the nanocrystals quickly reverted back to MT state after redispersion in toluene solvent. The *in situ* TEM heating experiment indicated that the recovery can be governed by surface recrystallization, and rapid nucleation and motion of twin boundaries.

ASSOCIATED CONTENT

Supporting Information.

The supporting information is available free of charge via the internet at https://pubs.acs.org.

- Detailed methods and experimental conditions with additional figures detailing data analysis, nanocrystal size distribution, simulated XRD patterns, TEM images, calculations for deviatoric stress and bulk modulus, derivation of thermodynamic MT to SC transition under pressure (PDF)
- TEM heating movie showing the nanocrystal twin boundary motion (MP4)

AUTHOR INFORMATION

Corresponding Author

*Corresponding author:

X. Wendy Gu

452 Escondido Mall, Room 227,

Stanford University, Stanford CA 94305

650-497-3189

xwgu@stanford.edu

Author Contributions

X.W.G. and A.P. conceived the idea and X.W.G. supervised the research of this work. A.P. synthesized the nanocrystals and M.T.K performed the TEM characterization. A.P., M.T.K., D.D., M.K. and A.D. performed the high-pressure XRD. A.P. performed the XRD simulation and analysis. S.L. and S.R. performed the MD simulations and analysis. A.P., S.L., S.R. and

X.W.G. wrote the manuscript. All authors have given approval to the final version of the manuscript.

Notes

Authors declare no competing financial interest.

ACKNOWLEDGMENT

X.W.G. and A.P. acknowledge financial support from the National Science Foundation under Grant No. DMR–2002936/2002891. The Advanced Light Source is supported by the Director, Office of Science, Office of Basic Energy Sciences, of the U.S. Department of Energy under Contract No. DE-AC02-05CH11231. Beamline 12.2.2 is partially supported by COMPRES, the Consortium for Materials Properties Research in Earth Sciences under NSF Cooperative Agreement EAR 1606856. Part of this work was performed at the Stanford Nano Shared Facilities (SNSF), supported by the National Science Foundation under award ECCS-1542152. M.T.K. is supported by the National Defense and Science Engineering Graduate Fellowship. D.D. is supported by the NSF Graduate Fellowship. S.L. and S.R. are supported by the Creative Materials Discovery Program (2016M3D1A1900038) through the National Research Foundation of Korea (NRF) funded by the Ministry of Science and ICT.

ABBREVIATIONS

XRD, X-ray Diffraction; DAC, diamond anvil cell; MD, molecular dynamics; TEM, transmission electron microscopy; SC, single crystalline; MT, multiply twinned.

306 REFERENCES

307 (1) Xia, Y.; Xiong, Y.; Lim, B.; Skrabalak, S. E. Shape-Controlled Synthesis of Metal
308 Nanocrystals: Simple Chemistry Meets Complex Physics? *Angew. Chem. Int. Ed.* **2009**,
309 *48* (1), 60–103. https://doi.org/10.1002/anie.200802248.

310 (2) Burda, C.; Chen, X.; Narayanan, R.; El-Sayed, M. A. Chemistry and Properties of
311 Nanocrystals of Different Shapes. *Chem. Rev*. **2005**, *105* (4), 1025–1102.
312 https://doi.org/10.1021/cr030063a.

313 (3) Goubet, N.; Yan, C.; Polli, D.; Portalès, H.; Arfaoui, I.; Cerullo, G.; Pileni, M. P.
314 Modulating Physical Properties of Isolated and Self-Assembled Nanocrystals through
315 Change in Nanocrystallinity. *Nano Lett.* **2013**, *13* (2), 504–508.
316 https://doi.org/10.1021/nl303898y.

317 (4) Uttam, P.; Kumar, V.; Kim, K. H.; Deep, A. Nanotwinning: Generation, Properties, and
318 Application. *Mater. Des*. **2020**, *192*, 108752.
319 https://doi.org/10.1016/j.matdes.2020.108752.

320 (5) Tang, Y.; Ouyang, M. Tailoring Properties and Functionalities of Metal Nanoparticles
321 through Crystallinity Engineering. *Nat. Mater.* **2007**, *6* (10), 754–759.
322 https://doi.org/10.1038/nmat1982.

323 (6) Huang, H.; Jia, H.; Liu, Z.; Gao, P.; Zhao, J.; Luo, Z.; Yang, J.; Zeng, J. Understanding of
324 Strain Effects in the Electrochemical Reduction of CO2: Using Pd Nanostructures as an
325 Ideal Platform. *Angew. Chem. Int. Ed.* **2017**, *56* (13), 3594–3598.
326 https://doi.org/10.1002/anie.201612617.

327 (7) Wang, X.; Choi, S. Il; Roling, L. T.; Luo, M.; Ma, C.; Zhang, L.; Chi, M.; Liu, J.; Xie, Z.;

Herron, J. A.; Mavrikakis, M.; Xia, Y. Palladium-Platinum Core-Shell Icosahedra with Substantially Enhanced Activity and Durability towards Oxygen Reduction. *Nat. Commun.* **2015**, *6*, 7594. https://doi.org/10.1038/ncomms8594.

(8) Xia, Y.; Gilroy, K. D.; Peng, H. C.; Xia, X. Seed-Mediated Growth of Colloidal Metal Nanocrystals. *Angew. Chem. Int. Ed.* **2017**, *56* (1), 60–95. https://doi.org/10.1002/anie.201604731.

(9) Baletto, F.; Ferrando, R. Structural Properties of Nanoclusters: Energetic, Thermodynamic, and Kinetic Effects. *Rev. Mod. Phys.* **2005**, *77* (1), 371–423. https://doi.org/10.1103/RevModPhys.77.371.

(10) Gruner, M. E.; Entel, P. Simulating Functional Magnetic Materials on Supercomputers. *J. Phys. Condens. Matter* **2009**, *21* (29), 31. https://doi.org/10.1088/0953-8984/21/29/293201.

(11) Sheng, H. W.; Luo, W. K.; Alamgir, F. M.; Bai, J. M.; Ma, E. Atomic Packing and Short-to-Medium-Range Order in Metallic Glasses. *Nature* **2006**, *439* (7075), 419–425. https://doi.org/10.1038/nature04421.

(12) Ino, S. Stability of Multiply-Twinned Particles. *J. Phys. Soc. Jpn.* **1969**, *27* (4), 941–953. https://doi.org/10.1143/JPSJ.27.941.

(13) Baletto, F.; Ferrando, R.; Fortunelli, A.; Montalenti, F.; Mottet, C. Crossover among Structural Motifs in Transition and Noble-Metal Clusters. *J. Chem. Phys.* **2002**, *116* (9), 3856–3863. https://doi.org/10.1063/1.1448484.

(14) Myshlyavtsev, A. V.; Stishenko, P. V.; Svalova, A. I. A Systematic Computational Study of the Structure Crossover and Coordination Number Distribution of Metallic

Nanoparticles. *Phys. Chem. Chem. Phys.* **2017**, *19* (27), 17895–17903. https://doi.org/10.1039/c6cp07571a.

(15) Plessow, P. N. The Transformation of Cuboctahedral to Icosahedral Nanoparticles: Atomic Structure and Dynamics. *Phys. Chem. Chem. Phys.* **2020**, *22* (23), 12939–12945. https://doi.org/10.1039/d0cp01651a.

(16) Vogel, W.; Bradley, J.; Vollmer, O.; Abraham, I. Transition from Five-Fold Symmetric to Twinned FCC Gold Particles by Thermally Induced Growth. *J. Phys. Chem. B* **1998**, *102* (52), 10853–10859. https://doi.org/10.1021/jp9827274.

(17) Gao, W.; Wu, J.; Yoon, A.; Lu, P.; Qi, L.; Wen, J.; Miller, D. J.; Mabon, J. C.; Wilson, W. L.; Yang, H.; Zuo, J. M. Dynamics of Transformation from Platinum Icosahedral Nanoparticles to Larger FCC Crystal at Millisecond Time Resolution. *Sci. Rep.* **2017**, *7*, 17243. https://doi.org/10.1038/s41598-017-16900-6.

(18) Ajayan, P. M.; Marks, L. D. Phase Instabilities in Small Particles. *Phase Transitions A Multinatl. J.* **1990**, *24-26* (1), 229–258. https://doi.org/10.1080/01411599008210232.

(19) Mackay, A. L. A Dense Non-Crystallographic Packing of Equal Spheres. *Acta Cryst.* **1962**, *15* (9), 916–918. https://doi.org/10.1107/s0365110x6200239x.

(20) Inasawa, S.; Sugiyama, M.; Yamaguchi, Y. Laser-Induced Shape Transformation of Gold Nanoparticles below the Melting Point: The Effect of Surface Melting. *J. Phys. Chem. B* **2005**, *109* (8), 3104–3111. https://doi.org/10.1021/jp045167j.

(21) Bovin, J. O.; Malm, J. O. Atomic Resolution Electron Microscopy of Small Metal Clusters. *Z. Phys. D : At., Mol. Clusters* **1991**, *19* (4), 293–298. https://doi.org/10.1007/BF01448314.

(22) Iijima, S.; Ichihashi, T. Structural Instability of Ultrafine Particles of Metals. *Phys. Rev. Lett.* **1986**, *56* (6), 616–619. https://doi.org/10.1103/PhysRevLett.56.616.

(23) Gilroy, K. D.; Puibasset, J.; Vara, M.; Xia, Y. On the Thermodynamics and Experimental Control of Twinning in Metal Nanocrystals. *Angew. Chem. Int. Ed.* **2017**, *56* (30), 8647–8651. https://doi.org/10.1002/anie.201705443.

(24) Dobson, D. P. Self-Diffusion in Liquid Fe at High Pressure. *Phys. Earth Planet. Inter.* **2002**, *130* (3–4), 271–284. https://doi.org/10.1016/S0031-9201(02)00011-0.

(25) Bai, F.; Bian, K.; Huang, X.; Wang, Z.; Fan, H. Pressure Induced Nanoparticle Phase Behavior, Property, and Applications. *Chem. Rev*. **2019**, *119* (12), 7673–7717. https://doi.org/10.1021/acs.chemrev.9b00023.

(26) Koski, K. J.; Kamp, N. M.; Smith, R. K.; Kunz, M.; Knight, J. K.; Alivisatos, A. P. Structural Distortions in 5-10 Nm Silver Nanoparticles under High Pressure. *Phys. Rev. B - Condens. Matter Mater. Phys.* **2008**, *78* (16), 165410. https://doi.org/10.1103/PhysRevB.78.165410.

(27) Parakh, A.; Lee, S.; Harkins, K. A.; Kiani, M. T.; Doan, D.; Kunz, M.; Doran, A.; Hanson, L. A.; Ryu, S.; Gu, X. W. Nucleation of Dislocations in 3.9 Nm Nanocrystals at High Pressure. *Phys. Rev. Lett.* **2020**, *124* (10), 106104. https://doi.org/10.1103/PhysRevLett.124.106104.

(28) Peng, S.; Lee, Y.; Wang, C.; Yin, H.; Dai, S.; Sun, S. A Facile Synthesis of Monodisperse Au Nanoparticles and Their Catalysis of CO Oxidation. *Nano Res.* **2008**, *1* (3), 229–234. https://doi.org/10.1007/s12274-008-8026-3.

(29) Jiang, Q.; Liang, L. H.; Zhao, D. S. Lattice Contraction and Surface Stress of Fcc

Nanocrystals. *J. Phys. Chem. B* **2001**, *105* (27), 6275–6277. https://doi.org/10.1021/jp010995n.

(30) Longo, A.; Martorana, A. Distorted f.c.c. Arrangement of Gold Nanoclusters: A Model of Spherical Particles with Microstrains and Stacking Faults. *J. Appl. Cryst.* **2008**, *41* (2), 446–455. https://doi.org/10.1107/S0021889808004846.

(31) Warren, B. E. X-Ray Measurement of Stacking Fault Widths in Fcc Metals. *J. Appl. Phys.* **1961**, *32* (11), 2428–2431. https://doi.org/10.1063/1.1777086.

(32) Herbst, C. A.; Cook, R. L.; King Jr., H. E. Density-Mediated Transport and the Glass Transition: High Pressure Viscosity Measurements in the Diamond Anvil Cell. *J. Non. Cryst. Solids* **1994**, *172–174* (1), 265–271. https://doi.org/10.1016/0022-3093(94)90445-6.

(33) Li, B.; Wen, X.; Li, R.; Wang, Z.; Clem, P. G.; Fan, H. Stress-Induced Phase Transformation and Optical Coupling of Silver Nanoparticle Superlattices into Mechanically Stable Nanowires. *Nat. Commun.* **2014**, *5*, 4179. https://doi.org/10.1038/ncomms5179.

(34) Wang, Z.; Schliehe, C.; Wang, T.; Nagaoka, Y.; Cao, Y. C.; Bassett, W. A.; Wu, H.; Fan, H.; Weller, H. Deviatoric Stress Driven Formation of Large Single-Crystal PbS Nanosheet from Nanoparticles and in Situ Monitoring of Oriented Attachment. *J. Am. Chem. Soc.* **2011**, *133* (37), 14484–14487. https://doi.org/10.1021/ja204310b.

(35) Li, B.; Bian, K.; Lane, J. M. D.; Salerno, K. M.; Grest, G. S.; Ao, T.; Hickman, R.; Wise, J.; Wang, Z.; Fan, H. Superfast Assembly and Synthesis of Gold Nanostructures Using Nanosecond Low-Temperature Compression via Magnetic Pulsed Power. *Nat. Commun.* **2017**, *8*, 14778. https:// doi.org/10.1038/ncomms14778.

(36) Cullity, B. D.; Stock, S. R. Elements of X-Ray Diffraction *Prentice Hall*, Upper Saddle River, **2014**.

(37) Song, M.; Zhou, G.; Lu, N.; Lee, J.; Nakouzi, E.; Wang, H.; Li, D. Oriented Attachment Induces Fivefold Twins by Forming and Decomposing High-Energy Grain Boundaries. *Science* **2020**, *367* (6473), 40–45. https://doi.org/10.1126/science.aax6511.

(38) Lim, T. H.; McCarthy, D.; Hendy, S. C.; Stevens, K. J.; Brown, S. A.; Tilley, R. D. Real-Time TEM and Kinetic Monte Carlo Studies of the Coalescence of Decahedral Gold Nanoparticles. *ACS Nano* **2009**, *3* (11), 3809–3813. https://doi.org/10.1021/nn9012252.

(39) José-Yacamán, M.; Gutierrez-Wing, C.; Miki, M.; Yang, D. Q.; Piyakis, K. N.; Sacher, E. Surface Diffusion and Coalescence of Mobile Metal Nanoparticles. *J. Phys. Chem. B* **2005**, *109* (19), 9703–9711. https://doi.org/10.1021/jp0509459.

(40) Chen, Y.; Palmer, R. E.; Wilcoxon, J. P. Sintering of Passivated Gold Nanoparticles under the Electron Beam. *Langmuir* **2006**, *22* (6), 2851–2855. https://doi.org/10.1021/la0533157.

(41) Howie, A.; Marks, L. D. Elastic Strains and the Energy Balance for Multiply Twinned Particles. *Philos. Mag. A Phys. Condens. Matter, Struct. Defects Mech. Prop.* **1984**, *49* (1), 95–109. https://doi.org/10.1080/01418618408233432.

(42) Wang, Y.; Teitel, S.; Dellago, C. Melting of Icosahedral Gold Nanoclusters from Molecular Dynamics Simulations. *J. Chem. Phys.* **2005**, *122* (21), 214722. https://doi.org/10.1063/1.1917756.

(43) Barreteau, C.; Desjonquères, M. C.; Spanjaard, D. Theoretical Study of the Icosahedral to Cuboctahedral Structural Transition in Rh and Pd Clusters. *Eur. Phys. J. D.* **2000,** *11* (3),

395-402. https://doi.org/10.1007/s100530070068.

(44) Wei, C. M.; Cheng, C.; Chang, C. M. Transition between Icosahedral and Cuboctahedral Nanoclusters of Lead. *J. Phys. Chem. B* **2006**, *110* (48), 24642–24645. https://doi.org/10.1021/jp063982o.

(45) Aragón, J. L. Transition from Multiply Twinned Icosahedral to Cuboctahedral Symmetry in Particles of Arbitrary Size. *Chem. Phys. Lett.* **1994**, *226* (3–4), 263–267. https://doi.org/10.1016/0009-2614(94)00722-5.

(46) Rollmann, G.; Gruner, M. E.; Hucht, A.; Meyer, R.; Entel, P.; Tiago, M. L.; Chelikowsky, J. R. Shellwise Mackay Transformation in Iron Nanoclusters. *Phys. Rev. Lett.* **2007**, *99* (8), 083402. https://doi.org/10.1103/PhysRevLett.99.083402.

(47) Angelié, C.; Soudan, J. M. Nanothermodynamics of Iron Clusters: Small Clusters, Icosahedral and Fcc-Cuboctahedral Structures. *J. Chem. Phys.* **2017**, *146* (17), 174303. https://doi.org/10.1063/1.4982252.

(48) Cheng, B.; Ngan, A. H. W. Thermally Induced Solid-Solid Structural Transition of Copper Nanoparticles through Direct Geometrical Conversion. *J. Chem. Phys.* **2013**, *138* (16), 164314. https://doi.org/10.1063/1.4802025.

(49) Li, G. J.; Wang, Q.; Liu, T.; Li, D. G.; Lu, X.; He, J. C. Molecular Dynamics Simulation of Icosahedral Transformations in Solid Cu - Co Clusters. *Chin. Phys. Lett.* **2009**, *26* (3), 036104. https://doi.org/10.1088/0256-307X/26/3/036104.

(50) Gao, Y.; Li, G.; Piao, Y.; Liu, S.; Liu, S.; Wang, Q. Size-Dependent Cuboctahedron-Icosahedron Transformations of Co-Based Bimetallic by Molecular Dynamics Simulation. *Mater. Lett.* **2018**, *232*, 8–10. https://doi.org/10.1016/j.matlet.2018.08.070.

(51) Singh, A. K. The Lattice Strains in a Specimen (Cubic System) Compressed Nonhydrostatically in an Opposed Anvil Device. *J. Appl. Phys.* **1993**, *73* (9), 4278–4286. https://doi.org/10.1063/1.352809.

Figures

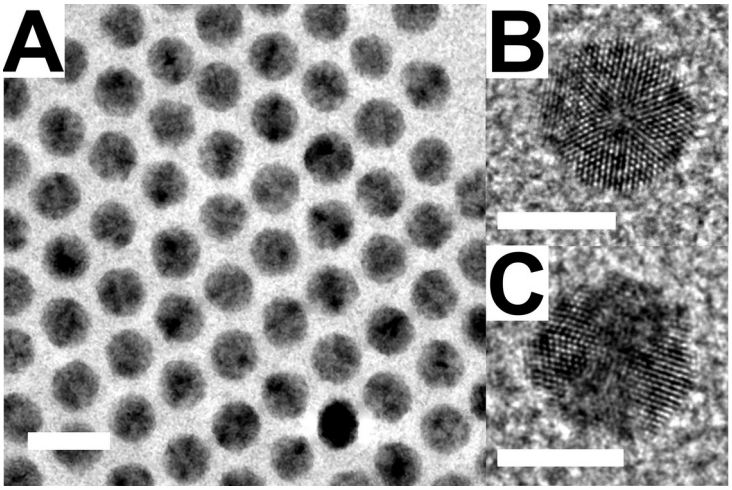

Fig. 1. TEM images of 6 nm Au nanocrystals. A) Bright field image of monodisperse nanocrystals. Scale bar is 10 nm. B, C) High-resolution images of icosahedral nanocrystals. Scale bar is 5 nm.

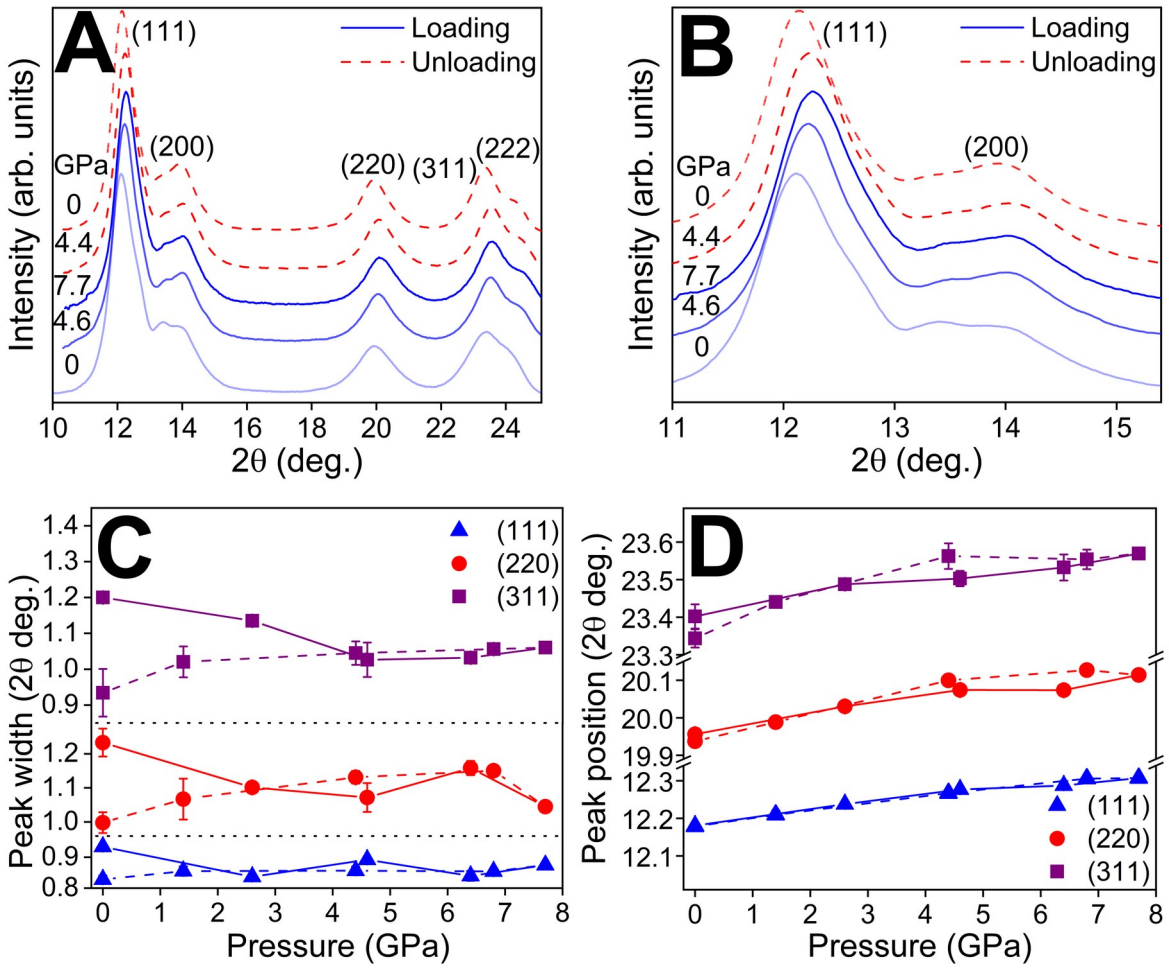

471

472 **Fig. 2. High-pressure XRD for 6 nm nanocrystals.** A) All diffraction peaks and B) magnified

473 view of (111) and (200) peaks. Change in diffraction peak C) width and D) position upon loading

474 (solid line) and unloading (dashed line).

475

476 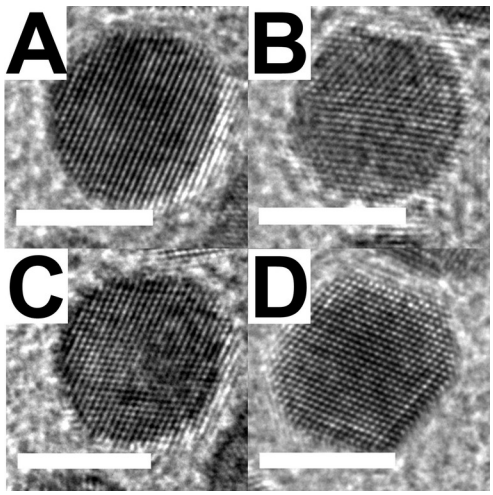

477 **Fig. 3. Post-compression TEM images of transformed single crystalline 6 nm nanocrystals.**

478

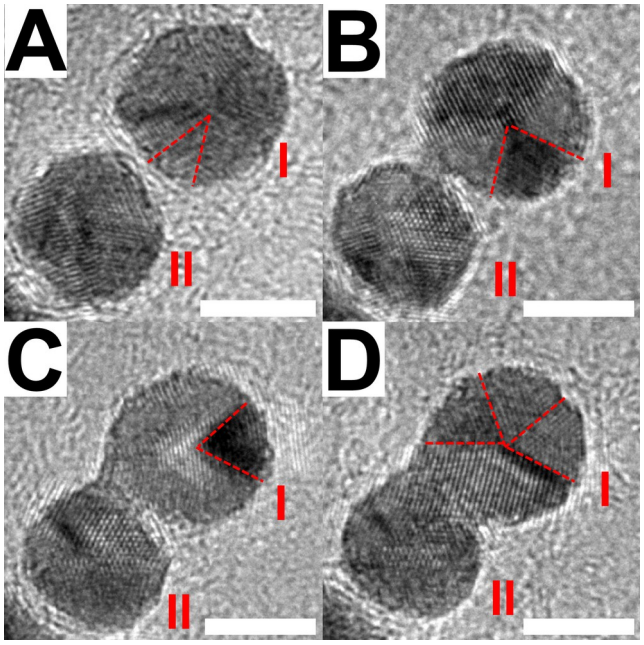

Fig. 4. Snapshots from *in situ* TEM movie showing coalescence of MT nanocrystals under electron irradiation. A) Nanocrystal I and II at the beginning of imaging and after B) 10 s, C) 40 s and D) 70 s of electron irradiation. Red dashed line denotes the twin boundary in nanocrystal I. Scale bar is 5 nm.

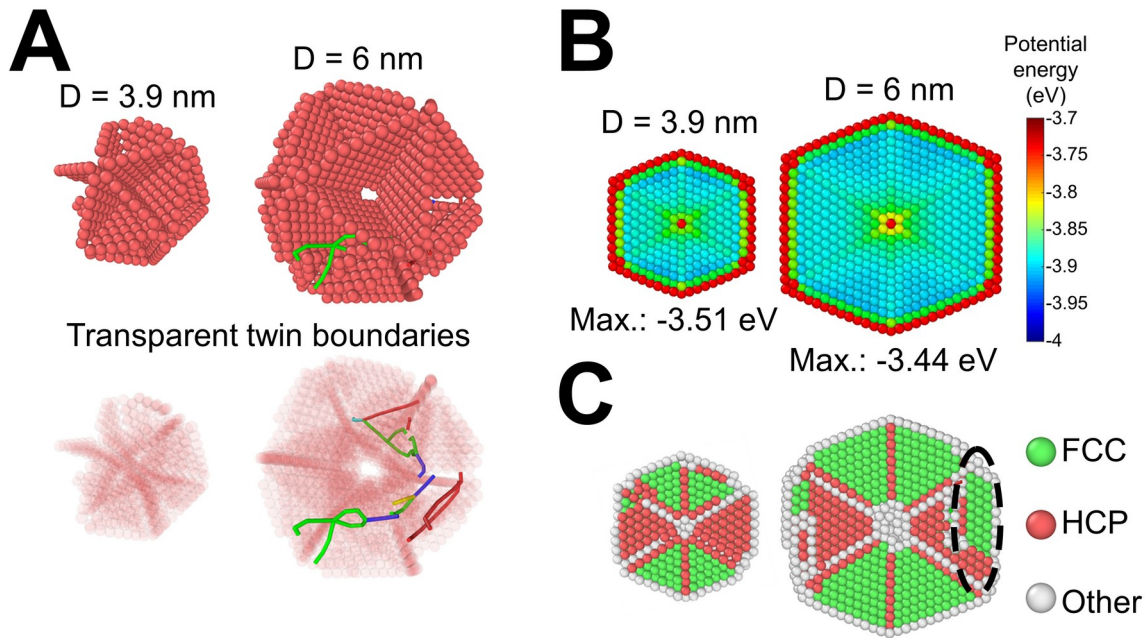

485

486 **Fig. 5. Atomistic simulation results of 3.9 nm and 6 nm icosahedral nanocrystals.** A) Twin
487 boundary and dislocation structures in icosahedral nanocrystals using high temperature MD
488 simulations. Dislocations are formed only in the 6 nm nanocrystal due to higher pre-stress.
489 (green lines: Shockley partial dislocation, blue lines: full dislocation, red lines: dislocation
490 blocked by twin boundaries). The red atoms are at twin boundaries. Atoms in regular FCC
491 crystal positions are removed for visualization purposes. B) The atomic potential energy of
492 pristine icosahedral nanocrystals. The 6 nm nanocrystal shows higher maximum potential energy
493 (equivalently, higher pre-stress). C) Crystal structures of the nanocrystals after high temperature
494 MD simulations. The twin boundary structure in 3.9 nm is preserved without noticeable
495 distortion, while the twin boundary structure in 6 nm undergoes significant distortion.

496

497 **ToC graphic**

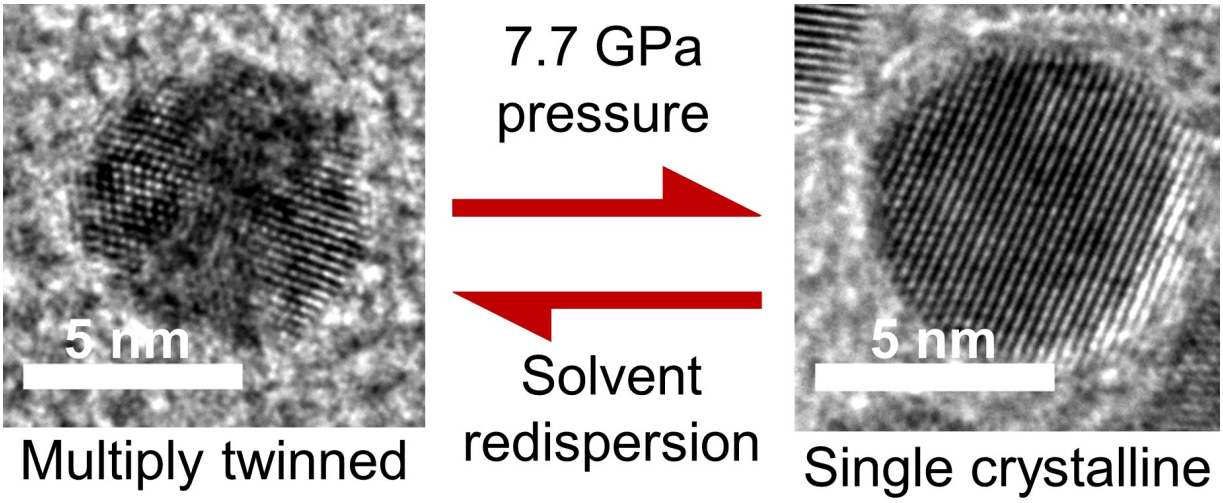

498